INTERNATIONAL JOURNAL FOR NUMERICAL METHODS IN FLUIDS
Int. J. Numer. Meth. Fluids 2001; **36**: 947–969 (DOI: 10.1002/fld.161)

Numerical simulation of the flow field in the vicinity of an axial flow fan

C. J. Meyer*,[1] and D. G. Kröger

Department of Mechanical Engineering, Matieland, South Africa

SUMMARY

The main purpose of the current investigation is the development and evaluation of a numerical model used to simulate the effect of an axial flow fan on the velocity field in the vicinity of the fan blades. The axial flow fan is modeled as an actuator disc, where the actuator disc forces are calculated using blade element theory. The calculated disc forces are expressed as sources/sinks of momentum in the Navier–Stokes equations solved by a commercially available computational fluid dynamic (CFD) code, Flo^{++}. The model is used to determine the fan performance characteristics of an axial flow fan as well as the velocity fields directly up- and downstream of the fan blades. The results are compared with experimental data. In general, good agreement is obtained between the numerical results and experimental data, although the fan power consumption, as well as radial velocity downstream of the fan blades, is underpredicted by the fan model. Copyright © 2001 John Wiley & Sons, Ltd.

KEY WORDS: actuator disc; axial flow fan; blade element theory

1. INTRODUCTION

An axial flow fan is a device that imparts a relatively small pressure rise to a continuously flowing gas. Axial flow fans are often employed as air pumps in systems that utilize ambient air for cooling purposes, as is evident in the prolific use of axial flow fans in industrial air-cooled heat exchangers.

The numerical investigation of the aerodynamic characteristics of systems that employ axial flow fans for cooling and other duties is an attractive alternative when considering the often prohibitive nature of experimental investigations due to economic and time constraints. The air flow-field through the axial flow fan blade passages, however, presents a formidable challenge to any numerical analysis tool.

Although quite a number of commercially available computational fluid dynamic (CFD) codes include special features to accommodate rotating blades, etc., there is a penalty to be

* Correspondence to: Private bag, Rondebosch 7701, South Africa.
[1] E-mail: cmeyer@eng.uct.ac.za

Received July 1999
Revised August 2000

paid in terms of computer processing power, computational grid complexity, and the time required to obtain a solution. The need for a model that accurately simulates the effect of a particular axial flow fan on the air flow field in the vicinity of the axial flow fan blades without imposing the constraints mentioned earlier is apparent.

In their numerical analysis of the flow field in chemical agitators, Pericleous and Patel [1] used an actuator disc model to simulate the effect of various forms of agitator blades on the flow field. Of particular interest is their use of the lift and drag characteristics of the agitator blade cross-sectional profiles at different radial stations to calculate the actuator disc forces. The actuator disc forces were expressed as sources/sinks of momentum in the Navier–Stokes equations, which were solved using a control volume formulation to yield the chemical agitator flow field. Good agreement is reported between the numerical results and experimental measurements.

A similar actuator disc model that utilizes blade element lift and drag characteristics in order to determine the actuator disc forces was developed by Thiart and Von Backström [2], and successfully used to determine the flow field in the vicinity of an axial flow fan subject to distorted inlet flow conditions.

Löstedt [3] simulated the effect of an aircraft propeller on the air flow field around an aircraft using an actuator disc model, where the actuator disc forces were determined with a combined momentum–blade element theory. Results compared favorably with experimental data.

Pelletier *et al.* [4–6] used actuator disc theory to predict the air flow field in the vicinity of a propeller in free stream. The flow field calculations were performed by solving the Navier–Stokes equations using a finite element formulation. The calculated actuator disc forces were included in the numerical scheme as momentum sources/sinks. The numerically predicted air flow field compared favorably with experimental data.

The current investigation presents the formulation of an axial flow fan model based on the actuator disc model developed by Pericleous and Patel [1]. The axial flow fan model is incorporated into a commercially available CFD code Flo^{++} through user programming, and was subsequently used to determine the fan performance characteristics of an axial flow fan of which the geometric details are known. The numerically determined fan performance characteristics, as well as the velocity field directly up- and downstream of the fan blades, are compared with experimental data. In order to facilitate a relatively small computational grid and short solution times, the fan exit geometry of the numerical model differs from the fan exit geometry for which the experimental fan performance characteristics are valid. The effect of the altered fan exit geometry on the fan performance characteristics is investigated experimentally.

2. COMPUTATIONAL MODEL

2.1. The governing equations

The following Reynolds-averaged conservation equations for steady, incompressible, and viscous fluid flows are solved in a Cartesian co-ordinate system by the CFD code. The equations are presented in Cartesian tensor notation [7] for the sake of brevity.

2.1.1. Conservation of mass. Mass conservation is expressed by

$$u_{j,j} = 0 \tag{1}$$

where u_j is the fluid velocity tensor.

2.1.2. Conservation of momentum. The Navier–Stokes equations for the conservation of momentum are given as

$$\rho u_i + (\rho u_j u_i - \tau_{ij})_{,j} = -p_{,i} + s_i \tag{2}$$

where ρ is the fluid density, τ_{ij} is the stress tensor, s_i is the momentum source tensor, and p is the static pressure.

The stress tensor τ_{ij} consists of the following terms:

$$\tau_{ij} = \mu(u_{i,j} + u_{j,i}) - \frac{2}{3}\mu u_{k,k}\delta_{ij} - \bar{\rho}\,\overline{u_i' u_j'} \tag{3}$$

where μ is the molecular dynamic fluid viscosity and δ_{ij} the Kronecker delta, which assumes unity when $i = j$ and zero otherwise. The turbulent Reynolds stresses are represented by the last term on the right-hand side of Equation (3) and contains the fluctuating part of the velocity tensor, u_i'.

2.1.3. Fluid turbulence model. The k–ε turbulence model of Launder and Spalding [8] is used to model the effects of turbulence on the fluid flow and temperature field. The additional turbulent stresses and heat flux terms are expressed, respectively as

$$-\bar{\rho}\,\overline{u_i' u_j'} = \mu_t(u_{i,j} + u_{j,i}) - \frac{2}{3}(\mu_t u_{k,k} + \rho k)\delta_{ij} \tag{4}$$

where μ_t is the fluid turbulent dynamic viscosity and k the turbulent kinetic energy defined as

$$k = \frac{\overline{u_i' u_i'}}{2} \tag{5}$$

The turbulent viscosity is linked to the turbulent kinetic energy and the dissipation rate of turbulent kinetic energy, ε, via

$$\mu_t = C_\mu \frac{\rho k^2}{\varepsilon} \tag{6}$$

where C_μ is a model constant.

The conservation equation for the turbulent kinetic energy is given as

$$\left(\rho u_j k - \frac{\mu_{\text{eff}}}{\sigma_k} k_{,j}\right) = \mu_t\left((u_{i,j} + u_{j,i})u_{i,j} - \frac{g_i}{\sigma_h \rho}\rho_{,i}\right) - \rho\varepsilon - \frac{2}{3}(\mu_t u_{i,i} + \rho k)u_{i,i} \tag{7}$$

where $\mu_{\text{eff}} = \mu + \mu_t$ and σ_k is a model constant.

The dissipation rate of the turbulent kinetic energy conservation equation is given as

$$\left(\rho u_j \varepsilon - \frac{\mu_{\text{eff}}}{\sigma_\varepsilon}\varepsilon_{,j}\right) = C_{\varepsilon 1}\frac{\varepsilon}{k}\left(\mu_t\left((u_{i,j} + u_{j,i})u_{i,j} - C_{\varepsilon 3}\frac{g_i}{\sigma_h \rho}\rho_{,i}\right) - \frac{2}{3}(\mu_t u_{i,i} + \rho k)u_{i,i}\right) - C_{\varepsilon 2}\rho\frac{\varepsilon^2}{k} - C_{\varepsilon 4}\rho\varepsilon u_{i,i} \tag{8}$$

where σ_ε, $C_{\varepsilon 1}$, $C_{\varepsilon 2}$, $C_{\varepsilon 3}$, and $C_{\varepsilon 4}$ are empirical coefficients.

The empirical coefficient values associated with the k–ε turbulence model are taken from References [8–10] and are listed in Table I.

2.2. Discretization practices

The CFD code used to perform the flow field calculations makes use of a finite volume formulation to discretize the governing partial differential equations (PDEs). A result of this particular formulation is that values for the different flow variables are required not only at computational cell centers but also at the boundary faces between adjacent cells. Various interpolation schemes have been developed to calculate the necessary flow variable values at cell boundaries from the known values at computational cell centers. The use of a particular interpolation scheme for a given computational grid is usually a compromise between numerical stability and accuracy.

The objective of the discretization process is to express the value of a scalar, ϕ, at a node, c, in the computational domain as a linear combination of the value of ϕ at a group of nodes in close proximity of node c so that

$$\phi_c = \sum_{n=1}^{N} a_n \phi_n \tag{9}$$

where a_n is the influence coefficient of the value of ϕ at the nth node of the group of nodes in close proximity of node c.

Table I. Values assigned to k–ε turbulence model coefficients.

C_μ	σ_k	σ_ε	$C_{\varepsilon 1}$	$C_{\varepsilon 2}$	$C_{\varepsilon 3}$	$C_{\varepsilon 4}$
0.09	1.00	1.22	1.44	1.92	1.44	−0.33

The influence coefficients of Equation (9) are a dependant of the conservation principle used to govern the behavior of ϕ within the calculation domain, the interpolation scheme used to determine scalar values, as well as scalar gradient values, at the cell boundaries, and also the geometrical characteristics of the individual cells comprising the calculation domain.

The current investigation makes use of the QUICK [11] interpolation scheme for the discretization of the momentum equations. The exclusive use of the QUICK scheme in the discretization of the turbulence model transport equations may produce non-physical negative values of the transport properties, which could lead to convergence problems. As a result, a linear blending of the QUICK scheme with a first-order up-wind (UD) scheme is used in the discretization of the turbulent transport equations, where the degree of blending is facilitated through the introduction of an adjustable blending factor, ψ.

A combination of the QUICK scheme with a UD scheme through the introduction of the blending factor ψ yields the following expression for ϕ_c:

$$\phi_c^{\text{Blended}} = (1-\psi)\sum_{n=1}^{M} a_n^{\text{QUICK}}\phi_n^{\text{QUICK}} + \psi\sum_{n=1}^{N} a_n^{\text{UD}}\phi_n^{\text{UD}} \tag{10}$$

where $0 \le \psi \le 1$.

2.3. The axial flow fan model

As stated earlier, the axial flow fan is modeled as an actuator disk. According to Von Mises [12], the force exerted on the fluid stream at any location within the actuator disk is a function of the fluid velocity vector relative to the fan blade, v_R, as well as the lift and drag characteristics of the fan blade cross-sectional profile. Figure 1 shows the relative velocity

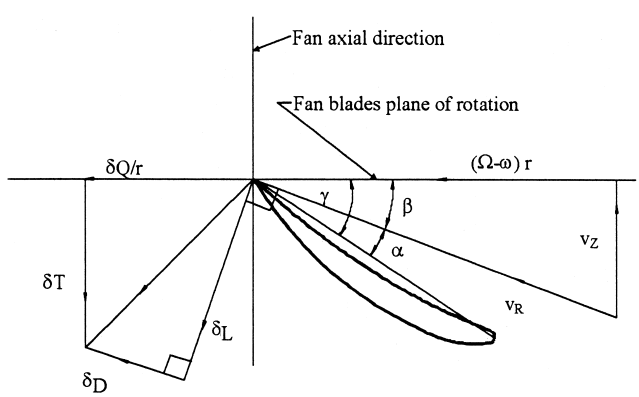

Figure 1. Blade element.

vector, v_R, as well as the resulting lift, δ_L, and drag force, δ_D, on a blade element at a fan blade radius r.

The lift and drag force are determined according to

$$\delta_L = \frac{1}{2}\rho |v_R|^2 C_l \cdot c_{Fb} \cdot \delta r \tag{11}$$

$$\delta_D = \frac{1}{2}\rho |v_R|^2 C_d \cdot c_{Fb} \cdot \delta r \tag{12}$$

where C_l and C_d are the coefficient of lift and drag respectively, c_{Fb} is the fan blade chord length, and δr is the blade element radial thickness.

The velocity field encountered by the two-dimensional blade elements of the axial flow fan model differs considerably from the uniform velocity field for which the lift and drag coefficients used in Equations (11) and (12) respectively are valid. The most notable difference being the tangential velocity component of the velocity field on the two-dimensional blade element downstream side. In order to compensate for this discrepancy, the relative velocity vector at the two-dimensional blade element is the average of the trailing edge velocity vector and the free-stream velocity vector upstream of the two-dimensional blade element. This arrangement is found to yield better results than the instance where the free-stream velocity vector upstream of the two-dimensional blade element alone is utilized to determine v_R.

From Figure 1 the blade element thrust, δT, and torque, δQ, are given as

$$\delta T = \delta L \cdot \cos\beta - \delta D \cdot \sin\beta \tag{13}$$

$$\delta Q = (\delta L \cdot \sin\beta + \delta D \cdot \cos\beta) \cdot r \tag{14}$$

where β is the angle between the relative velocity vector, v_R, and the fan blade plane of rotation. The blade forces are expressed as momentum sources/sinks in Equation (2), and the blade element thrust and torque need, therefore, to be expressed as force per unit volume. It follows that

$$\frac{\delta T}{\delta V} = \frac{n_{Fb} \cdot \delta T}{2\pi r \cdot \delta r \cdot t_{Fr}} = \frac{\sigma \cdot \delta T}{c_{Fb} \cdot \delta r \cdot t_{Fr}} \tag{15}$$

$$\frac{\delta Q}{\delta V} = \frac{n_{Fb} \cdot \delta T}{2\pi r \cdot \delta r \cdot t_{Fr}} = \frac{\sigma \cdot \delta Q}{c_{Fb} \cdot \delta r \cdot t_{Fr}} \tag{16}$$

where $\sigma = c_{Fb} n_{Fb}/2\pi r$ is the solidity ratio of the fan. Substitution of Equations (11)–(14) into Equations (15) and (16) yields

$$\frac{\delta T}{\delta V} = \frac{1}{2}\rho \overline{v_R}^2 \frac{\sigma}{t_{Fr}} (C_l \cdot \cos\beta - C_d \cdot \sin\beta) \tag{17}$$

$$\frac{\delta Q}{\delta V} = \frac{1}{2}\rho \overline{v_R}^2 \cdot r \cdot \frac{\sigma}{t_{Fr}} (C_l \cdot \sin\beta + C_d \cdot \cos\beta) \tag{18}$$

It only remains to calculate the coefficient of lift and drag to resolve Equations (17) and (18). Within a specified range of Mach numbers, the lift and drag characteristics of a profile section are a function of the Reynolds number and angle of attack, α, alone. With the angle between the fan blade chord and the plane of rotation of the fan blades, referred to as the stagger angle, γ, known at a particular radial station, the angle of attack can be calculated according to

$$\alpha = \gamma - \beta \tag{19}$$

Based on the design of the test fan, the lift and drag characteristics of the NASA-LS profile are used in the axial flow fan model. McGhee *et al.* [13] experimentally investigated the NASA-LS profile and plotted the dimensionless lift and drag coefficients, C_l and C_d, as a function of the angle of attack, α, for a range of Reynolds numbers. For angle of attack values falling outside of the range tested by McGhee *et al.* [13], the lift and drag characteristics for a flat plate are used. According to Hoerner and Borst [14] and Hoerner [15], the dimensionless lift and drag coefficient for a flat plate are given respectively as

$$C_l = C_{d_{max}} \cdot \sin\alpha \cdot \cos\alpha \tag{20}$$

and

$$C_d = C_{d_{max}} \cdot \sin^2\alpha \tag{21}$$

where $C_{d_{max}} = 1.98$.

A smooth transition between the NASA-LS and flat plate lift and drag characteristics is ensured with the introduction of fourth-order polynomial and trigometric functions in the overlap regions. Figure 2 displays the composite dimensionless lift and drag coefficient as a function of the angle of attack at a fan blade chord Reynolds number of 1.9×10^6 for the fan model. Linear interpolation is used to determine the C_l and C_d values at other Reynolds numbers.

3. GEOMETRY AND BOUNDARY CONDITIONS

3.1. Computational grid

This numerical investigation is an attempt to simulate the operation of the previously described axial flow fan (B-fan) in the test set-up shown schematically in Figure 3. In this particular test set-up, the B-fan is furnished with both inlet and outlet ducting. The inlet duct is of circular cross-section, while the outlet duct displays an annular cross-sectional profile. The inside diameter of the annular ducting at the fan outlet corresponds to the B-fan hub diameter. The computational grid is shown in Figure 4. Grid refinement in the radial, tangential, and axial directions is applied to cells in the vicinity of and within the actuator disc, where steep variable

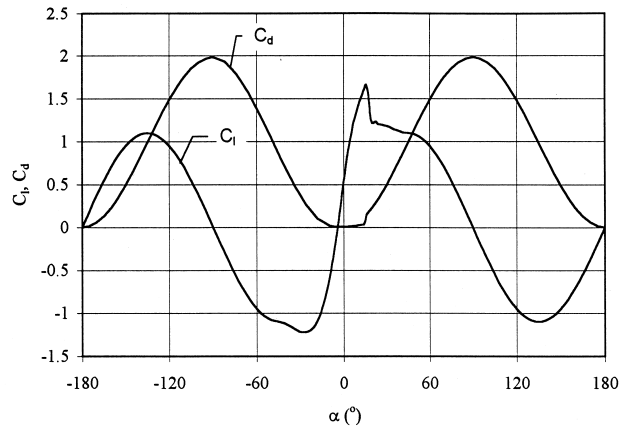

Figure 2. Composite dimensionless lift and drag coefficient of the fan blade cross-sectional profile, with $Re = 1.9 \times 10^6$.

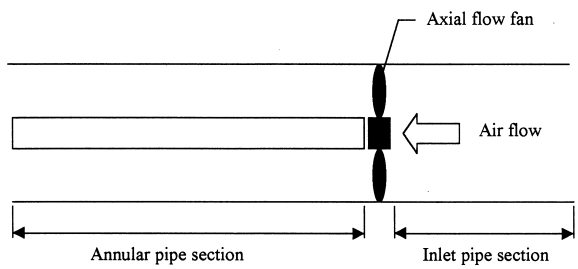

Figure 3. Geometry modeled by numerical analysis.

gradients are expected. Due to the axisymmetric nature of the problem only three computational cells are used in the grid tangential direction in areas where steep variable value gradients in the tangential direction are not expected.

3.2. Boundary conditions

The various boundary conditions applied to the cell faces on the exterior of the computational grid are displayed in Figure 4.

Uniform and constant values for the axial velocity field, the turbulent kinetic energy, k, and the dissipation rate of turbulent kinetic energy, ε, are specified at the indicated inlet boundary. Zero variable gradients are specified across the cell faces comprising the outlet boundary. Cyclic boundary conditions are applied to boundary cell faces that face in the computational grid tangential direction in order to preserve the axisymmetric nature of the flow field.

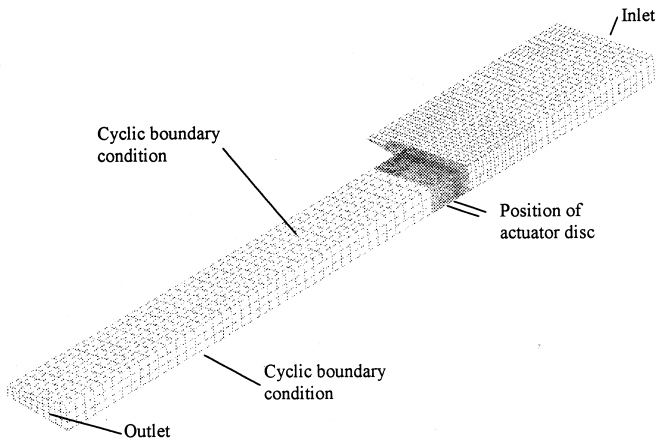

Figure 4. Computational grid.

Cyclic boundaries are pairs of geometrically identical boundary faces where the flow is repeated. The latter implies that scalar values, like temperature and pressure, for example, are identical at the corresponding points of a cyclic boundary pair, and that the Cartesian velocity components are also identical, apart from being rotated to ensure the same orientation relative to each of the boundary faces comprising the cyclic boundary pair.

A wall boundary condition is enforced on all other boundary cell faces.

4. EXPERIMENTAL EQUIPMENT AND PROCEDURE

4.1. Experimental equipment

Fan tests were conducted in a fan test facility designed according to the specifications of the British Standards Organization BS 848 [16] for type A tests (free inlet, free outlet). Figure 5 is a schematic representation of the fan test facility. The volume flow rate is measured at the calibrated inlet bell mouth (1) having a diameter of 1008 mm. The volume flow rate through the facility is controlled by means of a throttling device (3), with flow straighteners installed upstream (2) and downstream (4) thereof. Testing over a wider range of air volume flow rates is made possible with the use of a six-bladed auxiliary fan (5) with an outside diameter of 1540 mm located downstream of the throttling device. A third flow straightener (6) is located downstream of the auxiliary fan to remove the air rotational velocity component induced by the fan rotor. Flow guide vanes (7) are installed at the inlet of the settling chamber to distribute the air more evenly. The settling chamber inside dimensions are 4 m $\times$ 4 m $\times$ 7 m. A set of three stainless steel mesh screens (9) is installed within the settling chamber to insure a uniform velocity profile at the test fan (10) inlet. The outlet of the settling chamber takes on the form of a 2.5 m $\times$ 2.5 m square opening in which fan inlets can be installed for free outlet tests. The test fan (10) is driven by means of a hydraulic motor (11).

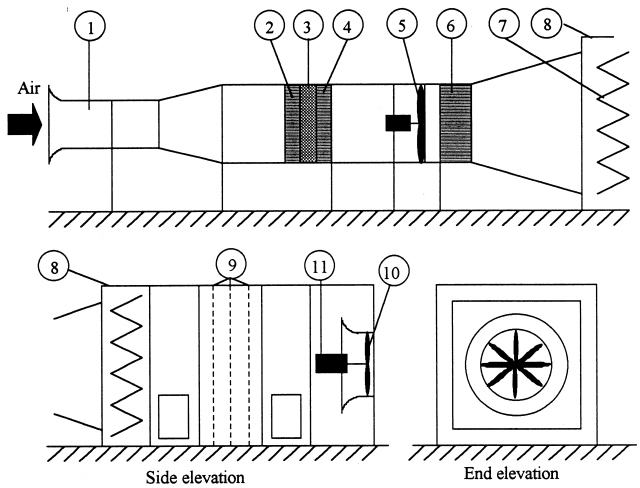

Figure 5. Schematic representation of the code fan test facility [80BS1].

The eight-bladed axial flow fan, hereafter referred to as the B-fan was designed and tested by Bruneau [17] and makes use of a NACA-LS blade cross-sectional profile. In general, the fan can be described as a medium chord axial flow fan, with both the blade chord and twist increasing from the blade tip reaching a maximum at the blade root close to the fan hub. The B-fan blades are molded glass fibre blades with a very smooth surface finish. Figure 6 is a schematic representation of the geometrical detail of the fan installation.

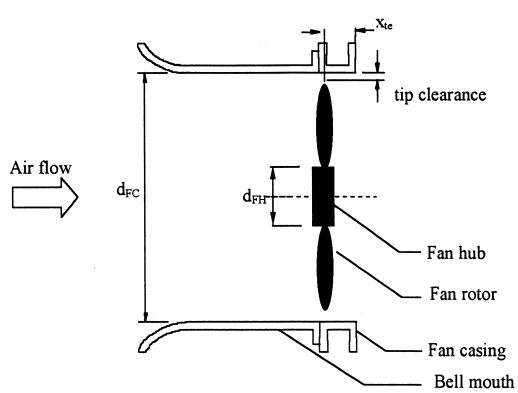

Figure 6. Fan installation geometrical detail.

Fan casing diameter, $d_{FC} = 1.542$ m
Hub diameter, $d_{FH} = 0.4$ m
Tip clearance, 4 mm
Blade tip trailing edge position, $x_{te} = 16$ mm
Rotational speed, $N = 750$ rpm

The geometrical characteristics of a representative fan blade were measured to determine the fan blade stagger angle, γ, and fan blade chord, c_{Fb}, distribution as a function of the diameter to fan casing diameter ratio, d/d_{FC}. Figure 7 displays the respective distributions.

4.2. Experimental procedure

The B-fan performance characteristics were determined with the axial flow fan and hydraulic motor drive in the position indicated in Figure 5. The performance test was repeated after the installation of an annular pipe section of length 3.5 m at the fan exit. The inside diameter of the annular pipe section corresponds to the fan hub diameter.

5. RESULTS AND DISCUSSION

5.1. Experimental investigation

The primary objective of the experimental investigation is to determine the effect that the addition of the annular pipe section at the fan exit has on the fan performance characteristics of the B-fan.

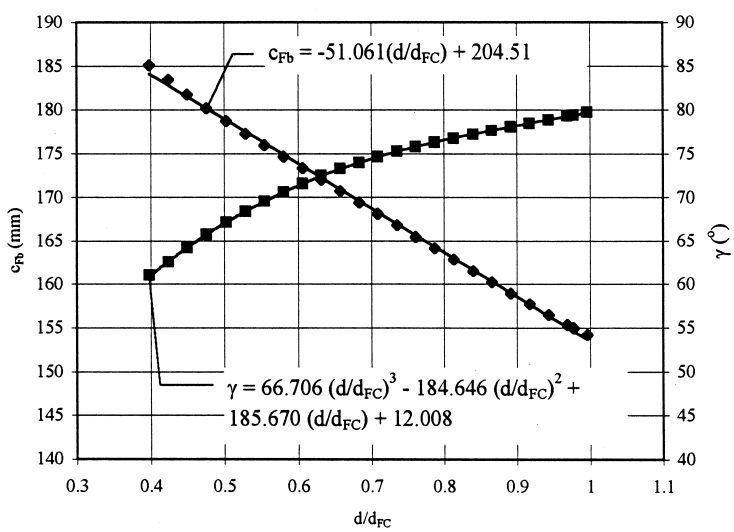

Figure 7. Fan blade chord and stagger angle distributions.

The fan performance characteristics are determined according to the specifications set in BS 848 [16] for a type A (free inlet, free outlet) installation and include the fan static pressure rise, Δp_{Fs}, the fan power consumption, P_R, and the fan static efficiency, η_{Fs} plotted as a function of the volume flow rate, V.

Figures 8–10 display the fan performance characteristics of the B-fan with and without the annular pipe section mounted at the fan outlet. The results indicate a very slight increase in the fan static pressure rise as well as the fan power consumption respectively with the addition of the annular pipe section. The fan static efficiency remains unaffected as is evident from the data displayed in Figure 10.

5.2. Numerical investigation

Figure 11 displays the four configurations for which fan performance characteristics are available. Figure 11(a) denotes the standard configurations as described in BS 848 [16], (b) denotes a modified configuration where a pipe section is installed between the inlet rounding and the axial flow fan, (c) displays the experimental set-up of the current investigation, where an annular pipe section is mounted at the fan exit, and finally (d) denotes the numerical model used in the current investigation.

Stinnes [18] experimentally investigated the performance characteristics of the B-fan over a range of blade angles in the standard configuration (Figure 11(a)) as well as the modified configuration (Figure 11(b)) and concluded that the fan performance characteristics are essentially unaffected by the differences between the two configurations.

The experimental results of the current investigation report a similar result when comparing the B-fan performance characteristics obtained utilizing configurations in Figure 11(a) and (c).

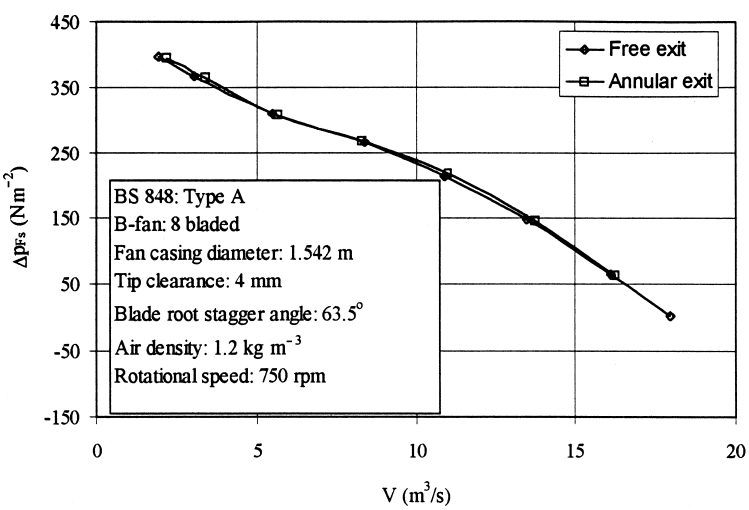

Figure 8. Δp_{Fs} versus V for a blade root stagger angle of 63.5°.

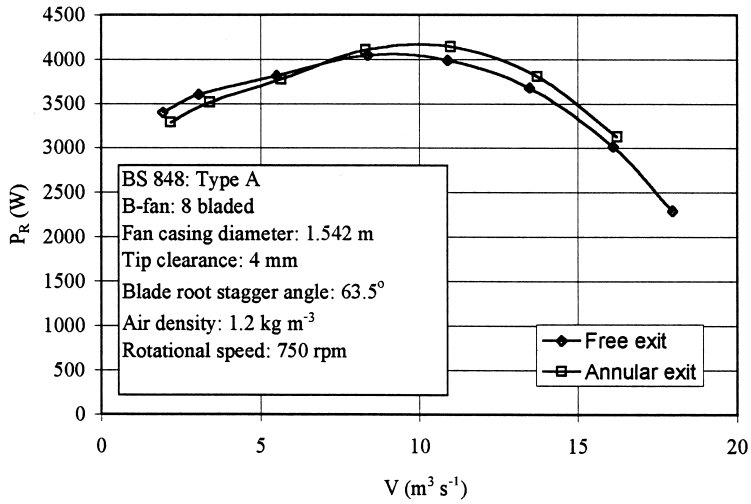

Figure 9. P_R versus V for a blade root stagger angle of 63.5°.

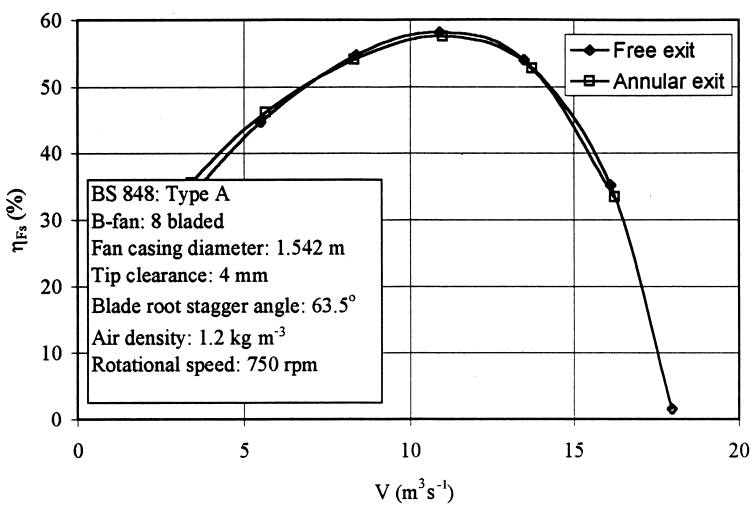

Figure 10. η_{Fs} versus V for a blade root stagger angle of 63.5°.

In light of the above it is reasonable to assume that the fan performance characteristics determined using a set-up similar to the configuration in Figure 11(d), where both fan inlet and outlet ducting are present, will not differ considerably from the results obtained using the standard configuration in Figure 11(a). As a result, a comparison between fan performance

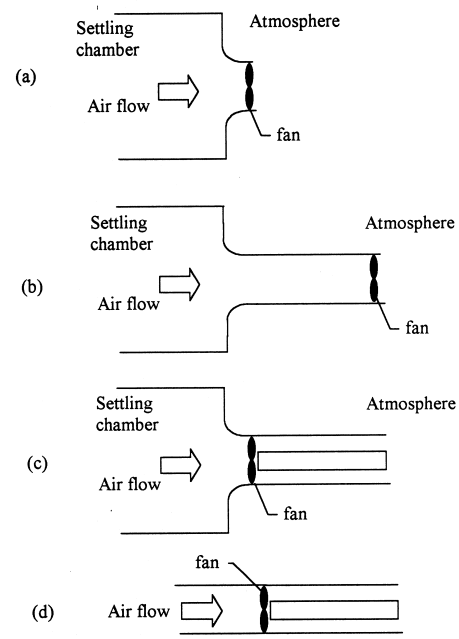

Figure 11. The different configurations of the fan test facility.

characteristics determined in the current numerical investigation utilizing a configuration similar to that depicted in Figure 11(d) and fan performance characteristics determined in the standard configuration of Figure 11(a) is considered an adequate measure to determine the accuracy of the axial flow fan model developed earlier.

Figures 12–23 display the fan performance characteristics of the B-fan determined experimentally by Bruneau [17] and Stinnes [18], as well as the fan performance characteristics determined from the results of the current numerical investigation. The results for four different blade angles are presented.

Figures 12–15 display the fan static pressure rise as a function of the air volume flow rate for the four fan blade settings. The static pressure rise determined by Stinnes [18] is slightly lower than that determined by Bruneau [17] for all four blade settings at volume flow rates in excess of 15 $m^3 s^{-1}$. Stinnes [18] attributes this discrepancy to slight differences in the fan hub geometry. The numerically determined static pressure characteristics are seen to follow the data of Bruneau [17] to high degree of accuracy.

The fan power consumption for the four fan blade settings tested is displayed in Figures 16–19. As in the case of the static pressure rise data, the fan power consumption supplied by Stinnes [18] is slightly lower than the values supplied by Bruneau [17]. The difference in the two sets of data can be attributed to the different experimental techniques applied by the two authors to account for the frictional torque of the fan motor drive train. Bruneau [17] also

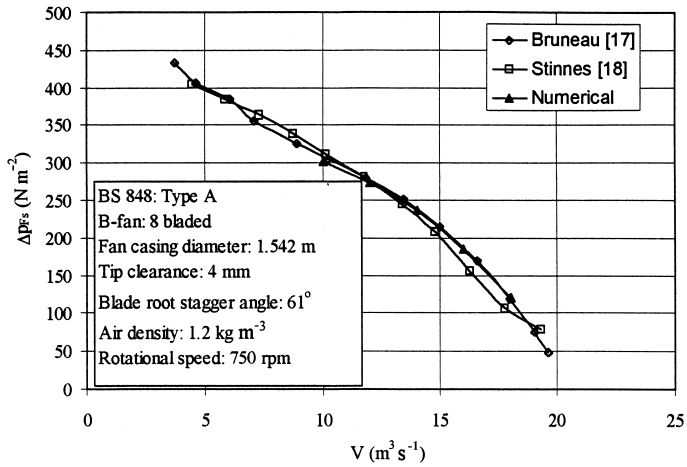

Figure 12. Δp_{Fs} versus V for a blade root stagger angle of 61°.

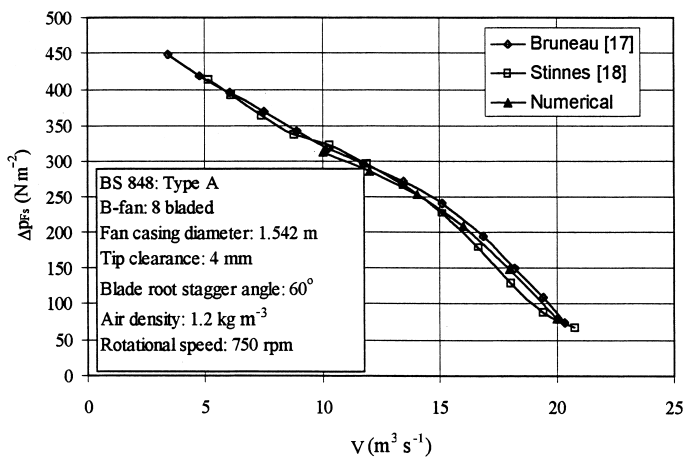

Figure 13. Δp_{Fs} versus V for a blade root stagger angle of 60°.

reports on discrepancies observed in measured torque values during repeatability tests. The numerically determined fan power consumption is lower than the experimental data. The latter is thought to be the result of the absence of any attempt to include the finite clearance between the fan blade tips and the fan ring in the numerical model. Although the additional tangential forces associated with blade tip clearance effects are arguably small they act over the length of the fan blade and could, as a result, have a significant effect on the calculated fan torque.

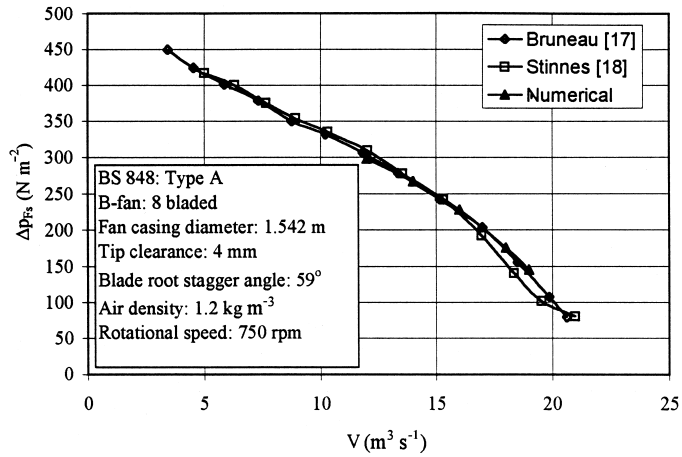

Figure 14. Δp_{Fs} versus V for a blade root stagger angle of 59°.

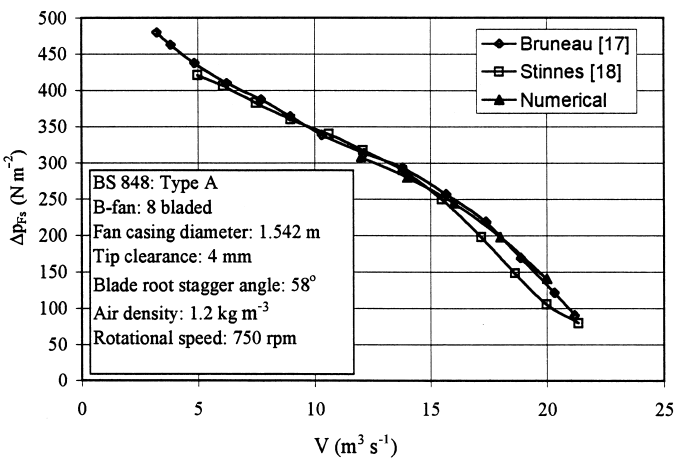

Figure 15. Δp_{Fs} versus V for a blade root stagger angle of 58°.

Figures 20–23 display the fan static efficiency of the fan blade settings tested. Due to the lower fan power consumption values associated with the numerically predicted fan performance characteristics, the numerically predicted fan static efficiency is slightly elevated above the data presented by Bruneau [17] and Stinnes [18]. The points of maximum fan static efficiency at a particular fan blade setting for the three sets of data all fall within a narrow air

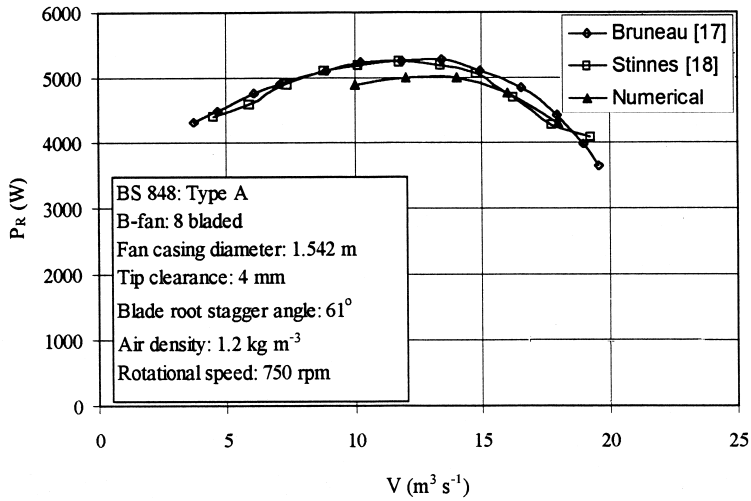

Figure 16. P_R versus V for a blade root stagger angle of 61°.

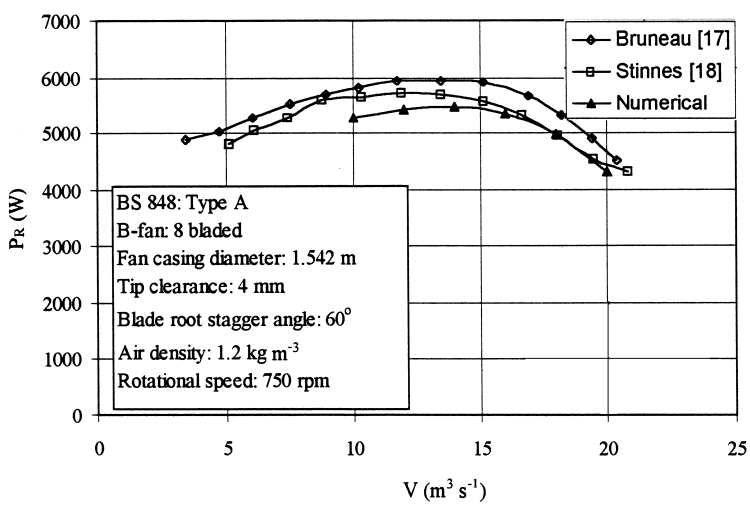

Figure 17. P_R versus V for a blade root stagger angle of 60°.

volume flow rate range of 1 $m^3 s^{-1}$. As in the case of the static pressure rise data, the numerically determined fan static efficiency curves seem to follow the data of Bruneau [17] more closely than that of Stinnes [18].

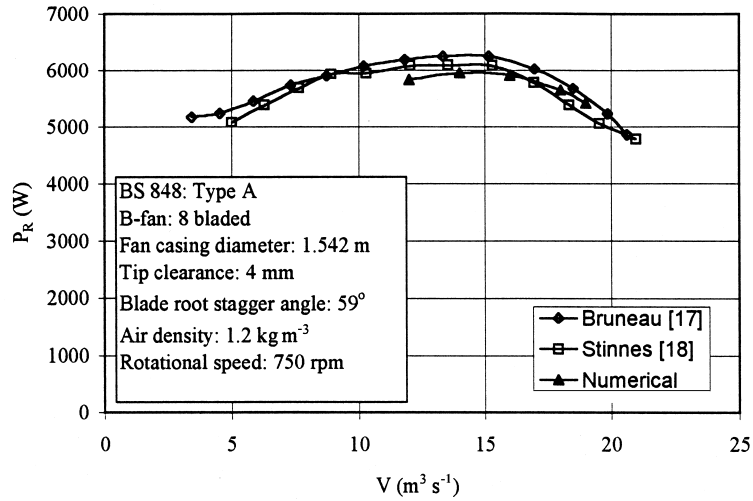

Figure 18. P_R versus V for a blade root stagger angle of 59°.

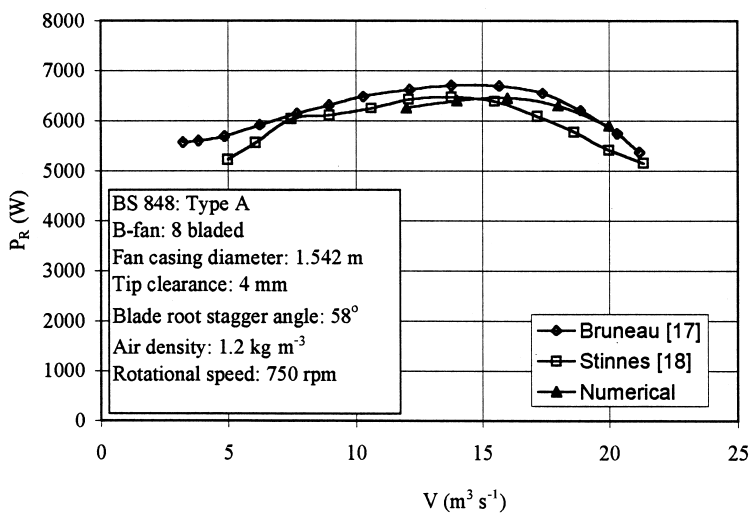

Figure 19. P_R versus V for a blade root stagger angle of 58°.

In his investigation of the B-fan performance characteristics, Stinnes [18] measured the velocity fields directly up- and downstream of the B-fan set at a blade root stagger angle of 60° and at a volume flow rate coinciding with the point of maximum fan static efficiency.

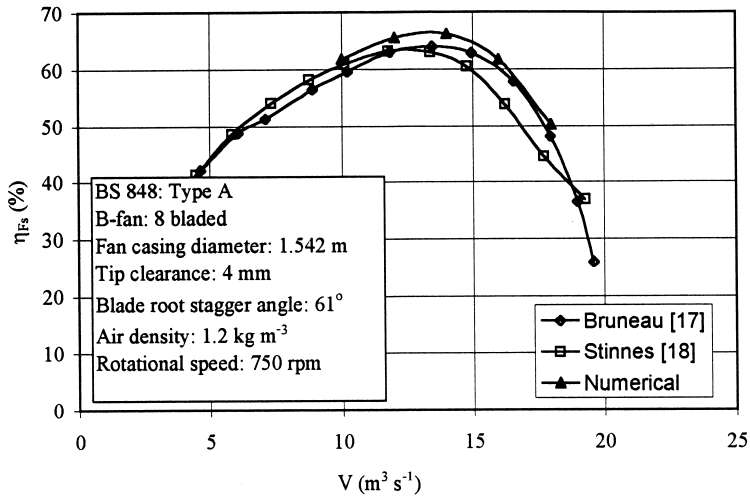

Figure 20. η_{Fs} versus V for a blade root stagger angle of 61°.

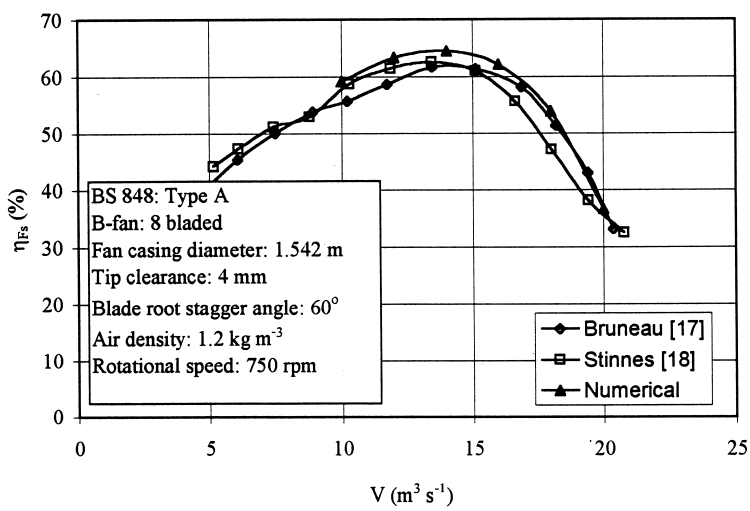

Figure 21. η_{Fs} versus V for a blade root stagger angle of 60°.

Although the exact location of the measurement planes are not given, comments by Stinnes [18] seem to indicate that the planes of measurement coincided with the upstream and downstream faces of the fan hub.

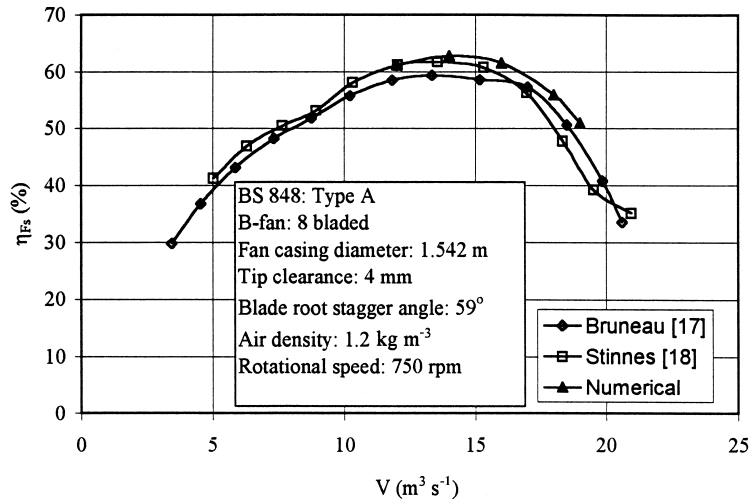

Figure 22. η_{Fs} versus V for a blade root stagger angle of 59°.

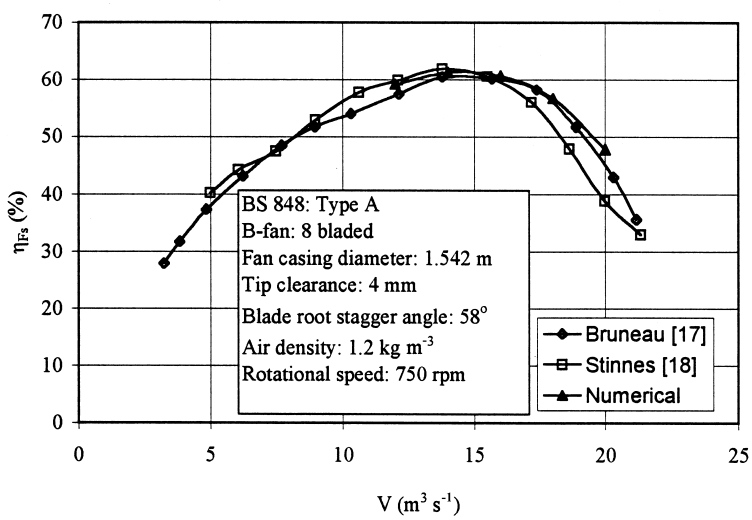

Figure 23. η_{Fs} versus V for a blade root stagger angle of 58°.

Figures 24 and 25 contrast the upstream and downstream velocity profiles determined from the results of the numerical analysis with the data of Stinnes [18]. Figure 24 indicates that the numerically determined upstream velocity profiles compare favorably with the experimental

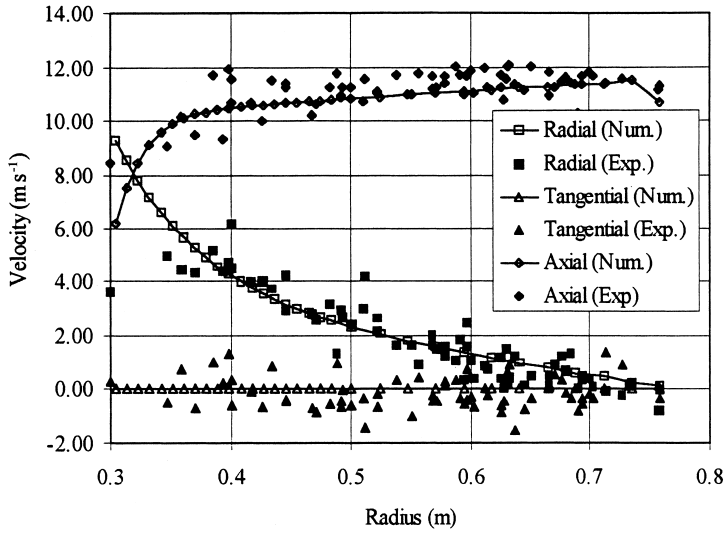

Figure 24. Velocity profiles directly upstream of the fan blades.

data. The numerically determined downstream velocity profiles displayed in Figure 25 appear to slightly underestimate the experimental data, although both the tangential and axial velocity profiles closely follow the trends of the experimental data. The numerically determined downstream radial velocity profile is seen to deviate from the trend suggested by the

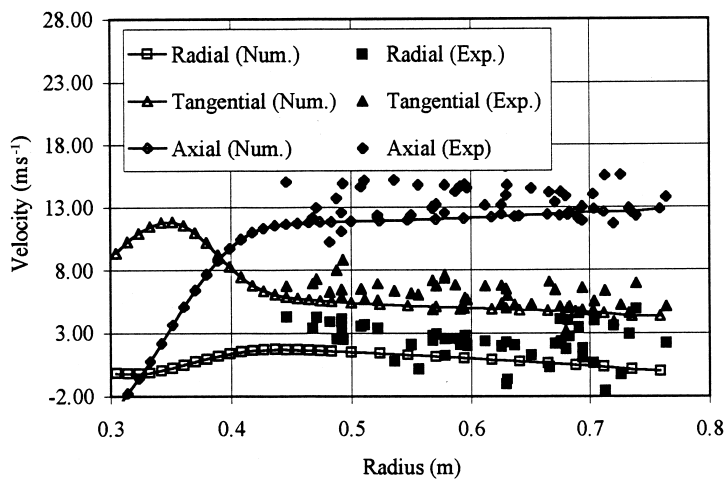

Figure 25. Velocity profiles directly downstream of the fan blades.

experimental data, especially in the region close to the fan hub. This is most likely a result of the inability of the fan model to account for radial forces exerted by the fan blades on the air stream. However, the difference between the experimentally and numerically determined fan downstream velocity profiles gives some indication of the relatively small effect on the downstream radial velocity profile of the radial forces exerted on the air stream by the fan blades in the experimental fan set-up. The effect of the latter is expected to be most noticeable in the region close to the fan hub as the flow across the fan blades experiences a force in the radial direction due to the presence of the fan hub.

6. CONCLUSIONS

A comparison of the numerical results with experimental data indicates the accuracy of the fan model in its prediction of the axial flow fan performance characteristics over a range of volume flow rates and blade settings. The numerically determined fan power consumption is shown to be slightly lower than the experimental data. This discrepancy is thought to be the result of the inability of the numerical analysis to include the effect of the finite clearance between the fan blade tips and the fan ring, which could lead to additional tangential forces. The numerically determined velocity fields directly up- and downstream of the axial flow fan also compares favorably with experimental data, although the downstream axial velocity field is slightly underpredicted by the numerical analysis. The downstream radial velocity profile is also seen to deviate from the trend suggested by the experimental data, especially in the region close to the fan hub. This deviation is attributed to the inability of the axial flow fan model to include any radial forces exerted on the fluid stream by the fan blades. The results, however, indicate that the radial forces are small compared with the axial and tangential forces exerted on the fluid stream by the axial flow fan blades.

REFERENCES

1. Pericleous KA, Patel MK. The modelling of tangential and axial agitators in chemical reactors. *PhysicoChemical Hydrodynamics* 1986; **8**(2): 105–123.
2. Thiart GD, von Backström TW. Numerical simulation of the flow field near an axial flow fan operating under distorted inflow conditions. *Journal of Wind Engineering and Industrial Aerodynamics* 1993; **45**: 189–214.
3. Löstedt P. Accuracy of a propeller model in inviscid flow. *Journal of Aircraft* 1995; **32**(6): 1312–1321.
4. Pelletier DH, Schetz JA. Finite element Navier–Stokes calculation of three-dimensional turbulent flow near a propeller. *AIAA Journal* 1986; **24**(9): 1409–1416.
5. Schetz JA, Pelletier D, Mallory DA. Experimental and numerical investigation of a propeller with three-dimensional inflow. *Journal of Propulsion* 1988; **4**(4): 341–349.
6. Pelletier D, Garon A, Camarero R. Finite element method for computing turbulent propeller flow. *AIAA Journal* 1991; **29**(1): 68–75.
7. Frederick D, Chang TS. *Continuum Mechanics*. Scientific Publishers: Cambridge, 1972.
8. Launder BE, Spalding DB. The numerical computation of turbulent flows. *Computational Methods in Applied Mechanics and Engineering* 1974; **3**: 269–289.
9. Rodi W. Influence of buoyancy and rotation on equations for turbulent length scale. In *Proceedings of 2nd Symposium on Turbulent Shear Flows*, 1979; 10.37–10.42.
10. El Tahry SH. k–ε equation for compressible reciprocating engine flows. *AIAA Journal of Energy* 1983; **7**(4): 345–353.
11. Leonard BP. A stable and accurate convective modelling procedure based on quadratic upstream interpolation. *Computer Methods in Applied Mechanics and Engineering* 1978; **19**: 59–98.

12. Von Mises R. *Theory of Flight*. McGraw-Hill: London, 1945.
13. McGhee RJ. Low-speed aerodynamic characteristics of a 17-percent-thick airfoil section designed for general aviation applications, N74-11821. Langley Research Center, December, 1973.
14. Hoerner SF, Borst HV. *Fluid-dynamic Lift*. Published by Mrs L.A. Hoerner: Brick Town, South Africa, 1975.
15. Hoerner SF. *Fluid-dynamic Drag*. Published by S.F. Hoerner: Brick Town, South Africa, 1965.
16. British Standards Institution. *Part 1: Methods of Testing Performance*. *Fans for General Purposes*, *BS 848*, 1980.
17. Bruneau PRP. The design of a single rotor axial flow fan for cooling tower application. Thesis for the degree of Master of Engineering (Mechanical), University of Stellenbosch, South Africa, 1994.
18. Stinnes W. An experimental investigation for rotor-only axial flow fans subject to a forced uniform cross-flow velocity component at inlet. Thesis for the degree of Master of Engineering (Mechanical), University of Stellenbosch, South Africa, 1999.

